

# Characterizing Asphalt Pavement 3-D Macrot texture Using Features of Co-occurrence Matrix

Yinghao Miao<sup>1+</sup>, Linbing Wang<sup>2</sup>, Xinfei Wang<sup>2</sup>, and Xiuqing Gong<sup>1</sup>

**Abstract:** This paper presents a method to characterize asphalt pavement macrot texture using the gray level co-occurrence matrix (GLCM). Data collected at 37 field sites are included in the analysis, representing 6 types of asphalt surface layers such as dense asphalt concrete (DAC), stone matrix asphalt (SMA), rubber asphalt concrete (RAC), ultra-thin wearing course (UTWC), micro-surfacing (MS), and open graded friction course (OGFC). This paper documents the investigation into the differences of GLCM indicators under various pixel pair spatial relationships. Then, the average of each GLCM indicator in some pixel pair spatial relationships is selected for mean texture depth (MTD) correlation. The correlation analysis shows there are 2 GLCM indicators,  $f_8$  and  $f_9$ , have strong relationship with MTD, which are entropy of the gray level sum distribution and the gray level combination distribution of pixel pairs of pavement macrot texture respectively. The larger the values of  $f_8$  and  $f_9$ , the more complex of the pavement macrot texture. The correlation coefficients between MTD and  $f_8, f_9$  are 0.9601 and 0.9493 respectively. The exponential models are better choice for connecting  $f_8$  and  $f_9$  with MTD, which are highly significant. The mean square errors (MSE) of the exponential models with  $f_8$  and  $f_9$  are 0.00343 and 0.00351 respectively.

**DOI:** 10.6135/ijprt.org.tw/2015.8(4).243

**Key words:** 3-D measurement; Asphalt pavement; GLCM; Macrot texture.

## Introduction

Pavement macrot texture is one of the major factors impacting pavement performances related to traffic safety, noise, and vehicle fuel economy [1-4]. Many researchers tried to quantify pavement macrot texture for improving its use in pavement evaluation. The development of three-dimensional (3-D) data acquisition techniques brings new solutions. Cackler et al. (2006) [5] developed a 3-D macrot texture collecting system, "RoboTex", and employed it to evaluate concrete pavement noise reduction methods. Abbas et al. (2007) [6] reconstructed the 3-D macrot textures of cement concrete pavement specimens from X-ray computerized tomography (CT) images. Ech et al. (2007) [7] acquired the 3-D surface data of asphalt mixture specimens before and after repeated loading tests using a laser based device in laboratory and then evaluated the durability of macrot texture. Gendy and Shalaby (2007) [8] developed a system to reconstruct pavement macrot texture in 3-D based on a four-source photometric stereo technique. They improved it in 2011 and named it as "PhotoTexture 2.0" [9]. Vilaca et al. (2009) [10] designed a 3-D macrot texture acquisition system, "TaxScan", using a laser triangulation technique. Wen (2009) [11] acquired 3-D data of pavement macrot texture using a 3-D optical scanner, XJTUOM, in laboratory. Some commercial 3-D laser scanners were also applied to collect pavement macrot texture data in laboratory and field [12, 13]. Some researchers developed

vehicle-mounted 3-D devices to achieve higher test speeds [14, 15].

The 3-D macrot texture measurements were often used to estimate texture (or profile) depth for comparing with the conventional indicators such as the mean texture depth (MTD) and the mean profile depth (MPD) [8, 13]. They were also used to quantify more detailed features of macrot texture by the fast Fourier transform (FFT), the wavelet analysis, etc. [6]. Though the new quantitative features enriched the pavement macrot texture evaluation, there is still room to introduce more options based on the 3-D digital measurements.

In the image processing field, texture analysis is usually used to extract features of image. When mapping the heights of a 3-D macrot texture onto a set of gray levels, an image of the macrot texture is obtained and then the image texture analysis methods can be applied for characterizing pavement 3-D macrot texture. Haralick et al. (1973) [16] introduced the gray-tone spatial-dependence matrix, now usually called gray level co-occurrence matrix (GLCM), for texture analysis, and then proposed 14 feature indicators. The GLCM based indicators are effective in extracting image texture features and widely applied in medical imaging, remote sensing, etc. [17-20]. They may be effective in capturing pavement macrot texture features.

This paper presents an investigation on how to quantify GLCM based features of asphalt pavement macrot texture from 3-D digital measurements collected in field for 6 types of surface layers of asphalt pavements. Then the relationships between the GLCM indicators and MTD are investigated. Some models connecting selected GLCM indicators with MTD are developed using regression analysis, which bridge the GLCM indicators with the practice.

## Background

<sup>1</sup> Beijing University of Technology, College of Metropolitan Transportation, 100 Pingleyuan, Chaoyang District, Beijing 100124 China.

<sup>2</sup> Virginia Polytechnic Institute and State University, 301N Patton Hall, Blacksburg, VA 24061 USA.

<sup>+</sup> Corresponding Author: E-mail miaoyinghao@bjut.edu.cn

Note: Submitted November 18, 2014; Revised April 24, 2015; Accepted May 2, 2015.

GLCM was proposed by Haralick et al. (1973) [16] and has been widely used for extracting texture features of image. It describes the frequencies or probabilities of the gray level combinations among the pixel pairs with given spatial relationship in a gray level image. The spatial relationship is usually defined by the distance between the centres of the 2 pixels (the pixel pair distance (PPD)) and the angle between the line connecting the centres of the 2 pixels and the horizontal direction (the pixel pair orientation (PPO)). There are 8 PPOs of 0°, 45°, 90°, 135°, 180°, 225°, 270°, and 315° generally considered, which correspond to the 8 immediate neighbors of a pixel in an image. Each 2 collinear orientations, such as 0° and 180°, could be combined into one orientation, which are suggested by Haralick (1979) [22]. The 4 major PPOs of 0°, 45°, 90°, and 135° are depicted in Fig. 1(a). A digital gray level image can be represented as  $I = \{G(x, y), x = 1, 2, \dots, N_x, y = 1, 2, \dots, N_y\}$ , where  $G(x, y)$  is the gray level at the location of  $(x, y)$ ,  $N_x$  and  $N_y$  are the pixel numbers at directions of  $x$  and  $y$  respectively. If an image has the maximum gray level of  $N_g$ , the GLCM in frequency can be defined as:

$$F_d^\theta(i, j) = \#\{[G(r, s), G(t, v)] : G(r, s) = i, G(t, v) = j\} \quad (1)$$

where # denotes the number of elements in the set,  $d$  is a given PPD,  $\theta$  is a given PPO,  $1 \leq i, j \leq N_g$  and, moreover,  $(t, v) = (r+d\cos\theta, s+d\sin\theta)$  or  $(t, v) = (r-d\cos\theta, s-d\sin\theta)$ . The GLCM in probability can be obtained through Eq. (2). Fig. 1(b) through Fig. 1(d) depicts the procedure for constructing a GLCM of an image.

$$P_d^\theta(i, j) = \frac{F_d^\theta(i, j)}{\sum_{m=1}^{N_g} \sum_{n=1}^{N_g} F_d^\theta(m, n)} \quad (2)$$

Haralick et al. (1973) [16] proposed 14 indicators based on GLCM for extracting texture features. Eqs. (3) and (5) are 2 GLCM indicators selected for developing relationship with MTD of pavement macrotexture (elaborated in section 5). The references [16, 23, 24] can be referred to for the other GLCM indicators.

$$f_8 = -\sum_{k=2}^{2N_g} P_{x+y}(k) \log(p_{x+y}(k)) \quad (3)$$

where

$$P_{x+y}(k) = \sum_{\substack{i=1 \\ i+j=k}}^{N_g} \sum_{j=1}^{N_g} P_d^\theta(i, j) \quad (4)$$

$$f_9 = \sum_{i=1}^{N_g} \sum_{j=1}^{N_g} P_d^\theta(i, j) \log(p_d^\theta(i, j)) \quad (5)$$

In fact, the GLCM of an image is the probability distribution of the gray level combination of pixel pairs with given spatial relationship, while  $P_{x+y}(k)$  is the probability distribution of the gray level sum of pixel pairs in accordance with Eq. (4). So  $f_8$  and  $f_9$  are entropy of the gray level sum distribution and the gray level combination distribution of pixel pairs respectively, which describe the average amount of information of the corresponding distribution.

According to Eq. (2), the GLCM depends on the values of PPO except that the image is statistically rotation invariant. Averaging the values derived from various PPOs for each GLCM indicator is a common approach to balance the effect of PPO. The PPD also has effect on GLCM in accordance with Eq. (2). Many researchers discussed how to choose the value of PPD for an analysis. Weszka et al. (1976) [25] found indicators with small PPD (1 or 2 pixels) are more powerful for terrain classification. Zucker and Terzopoulos (1980) [26] proposed a chi-square test method to determine the value of PPD that best captures the structure of texture. Connors and Harlow (1980) [27] found that the Markov textures considered in the research can be better discriminated when using multiple PPDs. Holmes et al. (1984) [28] applied a PPD of 2 pixels in sea ice classification. Chen et al. (1989) [29] found a PPD below 8 pixels has better classification accuracy for cloud field classification. Nystuen and Garcia Jr. (1992) [30] selected a PPD of 4 pixels because it is the shortest one which shows promising separation of the sea ice types in the research. Soh and Tsatsoulis (1999) [20] indicated a single PPD value is not enough for the image texture analysis of sea ice. They considered the mean over GLCMs derived from various PPD values a better option. Clausi (2002) [17] selected a PPD of 1 pixel for sea ice classification with a review of the related work. Many studies used a PPD of 1 pixel without detailed discussion [23, 31, 32]. According to the aforementioned review, it can be found that there is no common approach to pick out the proper value of PPD. Meeting the demand of specific application is a principle for determining the value of PPD.

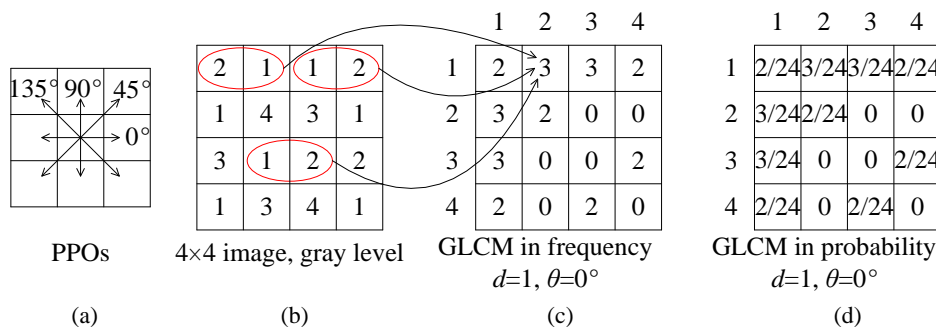


Fig. 1. The PPOs and the Calculation Method of GLCM.

**Table 1.** Basic Information of the Test Sites.

Highway Code	Grade	Surface Type			NMPS (mm)	Number of Test Sites	Opening Date
		Type	Sub-type	Alias			
G101	1	SMA	/	S	13.2	5	Aug. 2010
G101	1	UTWC	1	U1	9.5	4	Sept. 2009
G101	1	UTWC	2	U2	9.5	4	Sept. 2010
G101	1	MS	/	M	9.5	4	Sept. 2009
G111	2	DAC	1	D1	16	7	Jul. 2010
G111	2	RAC	/	R	16	6	Sept. 2010
X011	3	DAC	2	D2	13.2	3	Sept. 2009
JCXL	Urban Road	OGFC	/	O	13.2	4	Jun. 2008

**Field Data Collection**

Field tests were conducted at 37 sites which are selected from highways of different grades and urban roads in Huairou and Chaoyang District, Beijing, China. There are 6 types of asphalt surface layers from the 37 sites, including dense asphalt concrete (DAC), stone matrix asphalt (SMA), rubber asphalt concrete (RAC), ultra-thin wearing course (UTWC), mirco-surfacing (MS), and open graded friction course (OGFC). The basic information of the test sites is listed in Table 1. Each test site is given an ID according to its highway code, followed by the type of surface layer and a sequence number, such as G101-SMA-3. These tests were conducted in situ in November 2010 (tests on OGFC were done in May 2012).

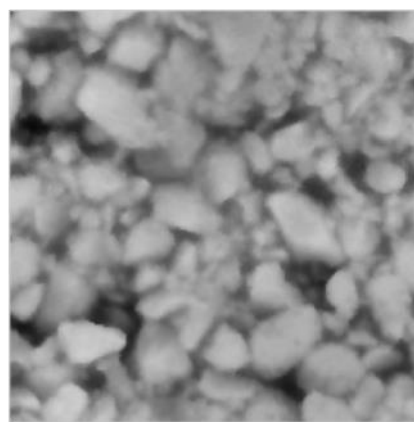
Pavement surface is scanned using a commercial hand-held 3-D laser scanner. The macrotexture is presented by a point set with the sample size of 90 mm×90 mm and at an interval of 0.5 mm in 2 horizontal directions. The test method is elaborated in another paper [21]. Fig. 2(a) gives an image of a real pavement surface and the corresponding collected macrotexture is depicted in Fig. 2(b). MTD was also collected using sand patch method (ASTM E965).

**Analysis of 3-D Macrotexture of Asphalt Pavement**

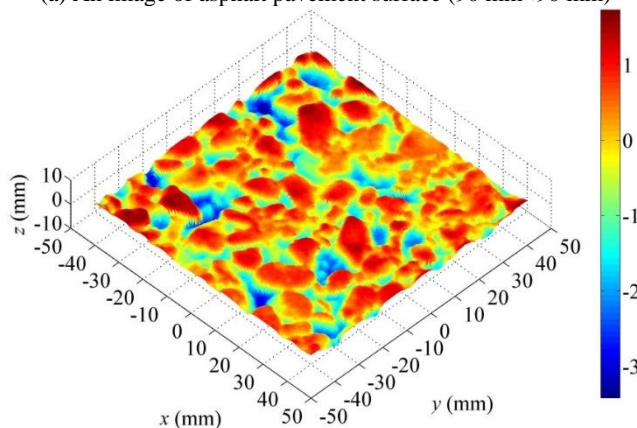
Firstly, the 3-D macrotexture measurement should be converted into a gray-level image via dividing the height range into sections using a given interval and mapping the height of each section onto a gray



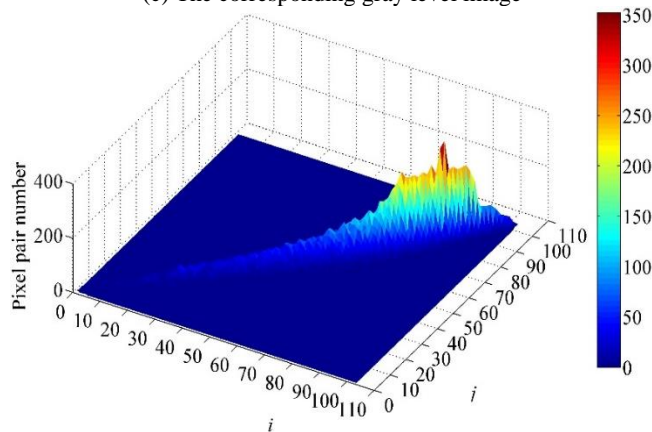
(a) An image of asphalt pavement surface (90 mm×90 mm)



(c) The corresponding gray level image



(b) The corresponding 3-D macrotexture



(d) The corresponding GLCM image

**Fig. 2.** Images of Various Scenarios for Macrotexture Evaluation.

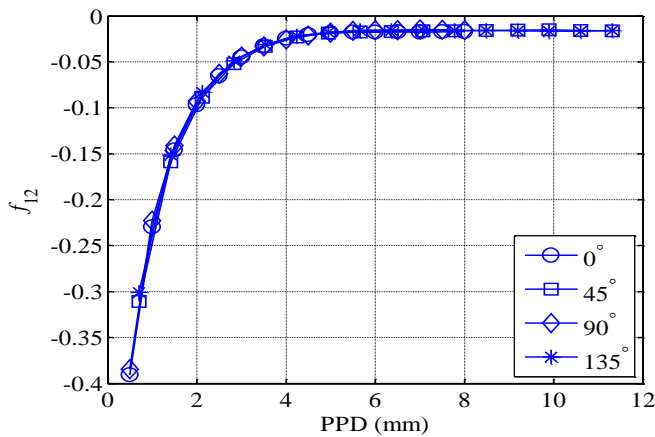


**Fig. 3.** A Typical GLCM Indicator Plot with the 4 PPOs.

level. Then, it can be characterized by GLCM indicators. This work employs an interval of 0.05 mm, which is the accuracy in depth of the 3-D scanner. The conversion can be described as Eq. (6).

$$G(x, y) = \text{floor}\left(\frac{Z(x, y) - \min(z)}{0.05}\right) + 1 \quad (6)$$

where  $(x, y)$  is the location of the point or pixel in the macrotexture;  $Z(x, y)$  is the height in mm at location  $(x, y)$ ,  $\text{floor}(\cdot)$  rounds a number to the nearest integer less than or equal to it. Fig. 2(c) depicts the gray level image corresponding to the macrotexture shown in Fig. 2(b). Fig. 2(d) shows the GLCM in frequency with PPD of 0.5 mm and PPO of 0° of the image.

In this investigation, all 14 GLCM indicators with 4 PPOs of 0°, 45°, 90°, and 135° and various PPDs were calculated to investigate the effects of PPO and PPD. The comparisons show there is no significant impact of PPO on all GLCM indicators of pavement macrotexture (Fig. 3 shows an example.). The reason is that asphalt pavement surface is statistically rotation invariant. Nevertheless, this work takes the average over 2 PPOs of 0° and 90° as the final value of each indicator (the other 2 PPOs do not have the same PPDs.). There are 2 GLCM indicators, i.e.,  $f_4$  and  $f_6$ , whose values do not significantly depend on PPD. Fig. 4(a) plots the typical relationships between  $f_4$  and PPD of the 6 types of pavements. The other indicators change to some extent with the increase of PPD and gradually reach steady values like  $f_5$  (Fig. 4(b)). So this work calculates all 14 GLCM indicators using PPDs of 0.5 mm through 8 mm by 0.5 mm (1 through 16 pixels) for the following analysis.

A correlation analysis is performed to investigate the relationships between the GLCM indicators derived from various PPDs and MTD. Fig. 5 depicts the changes of the correlation coefficients between the GLCM indicators and MTD with the increase of PPD. The correlation coefficients between  $f_3, f_{12}, f_{13}, f_{14}$ , and MTD are significantly PPD dependent, which are relatively low. The other GLCM indicators have relatively stable correlation coefficients with MTD among various PPDs except some slight changes in the PPD range between 0.5 mm and 2 mm. This paper takes the averages over PPDs between 0.5 mm and 2 mm for all GLCM indicators for the following analysis. Table 2 lists the correlation coefficients between the 14 GLCM indicators and MTD. There are 8 GLCM indicators have correlation coefficients above

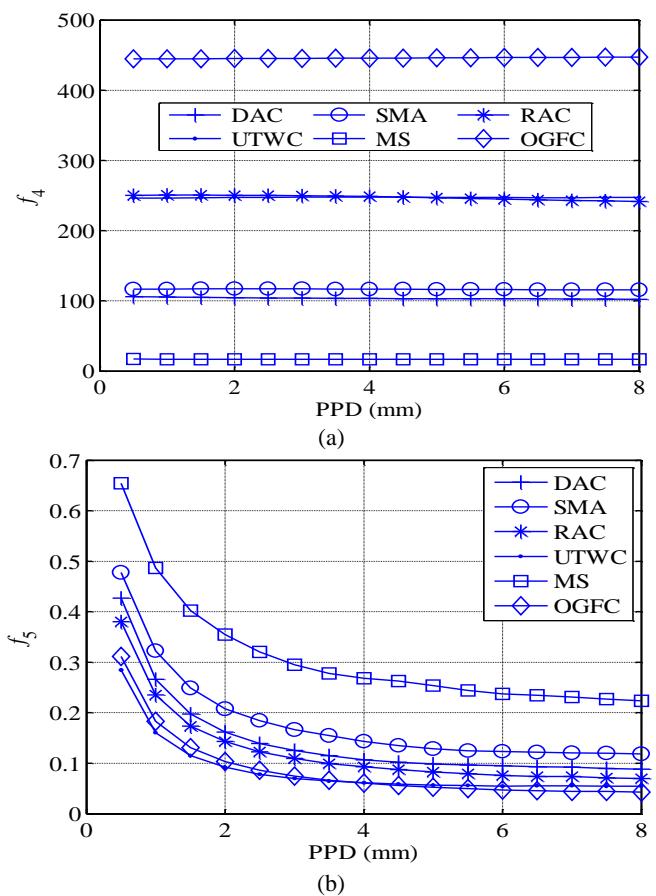


**Fig. 4.** Typical Plots of GLCM Indicators with Various PPDs.

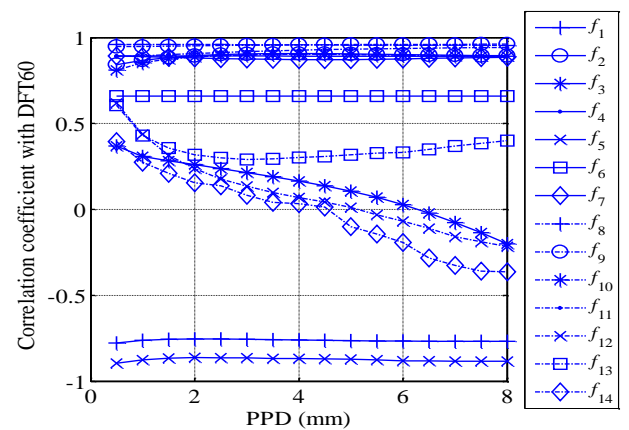


**Fig. 5.** Correlation Coefficients between MTD and each GLCM Indicator with Various PPDs.

**Table 2.** Pearson Correlation Coefficients between MTD and GLCM Indicators.

Indicators	MTD	Indicators	MTD
$f_1$	-0.7651	$f_8$	0.9601
$f_2$	0.8853	$f_9$	0.9493
$f_3$	0.2840	$f_{10}$	0.8748
$f_4$	0.8931	$f_{11}$	0.8985
$f_5$	-0.8766	$f_{12}$	0.4396
$f_6$	0.6598	$f_{13}$	0.3708
$f_7$	0.8872	$f_{14}$	0.2093

0.85 with MTD. Table 3 lists the values of the 8 GLCM indicators and MTD for all test sites.

### Development of Relationship between the GLCM Indicators and MTD

According to Table 2, there are 2 GLCM indicators,  $f_8$ , and  $f_9$ , between which and MTD the correlation coefficients are above 0.9. Fig. 6 presents the values and the means of  $f_8$ ,  $f_9$  and MTD sorted by the type of surface layer. Fig. 7 gives the scatter plots of MTD with  $f_8$  and  $f_9$ . According to the average values of  $f_8$  and MTD of each surface type, an ascending order is shown as MS, DAC2, DAC1, UTWC1, SMA, UTWC2, RAC, and OGFC in Fig. 6(a) and Fig. 6(c). For  $f_9$ , the order is similar except the switch of UTWC2 and RAC in Fig. 6(b). However, surface type cannot be clearly separated by each indicator alone except MS and OGFC.

Some relationships between the 2 GLCM indicators and MTD are analyzed using the regression method. Firstly, linear models are obtained as Eqs. (7) and (8). The analysis of variance for the linear models with  $f_8$  and  $f_9$  are presented in Tables 4 and 5 respectively. It is shown that the 2 models are highly significant. The mean square errors (MSE) of the models with  $f_8$  and  $f_9$  are 0.00451 and 0.0057 respectively and the R-squares are 0.9218 and 0.9011 respectively.

$$MTD = 0.4611f_8 - 1.1423 \quad (7)$$

$$MTD = 0.2426f_9 - 0.7343 \quad (8)$$

This work also investigates the exponential model in accordance with the scatter plots of the 2 GLCM indicators vs. MTD. Eqs. (9) and (10) are the exponential models. The analysis of variance for the

**Table 3.** Test Data of MTD and Some GLCM Indicators.

ID	Type Alias	MTD	$f_2$	$f_4$	$f_5$	$f_7$	$f_8$	$f_9$	$f_{10}$	$f_{11}$
G111-DAC-1	D1	0.725	27.503	74.011	0.297	268.543	4.139	6.238	13.065	2.273
G111-DAC-2	D1	0.905	37.998	105.329	0.263	383.318	4.369	6.652	17.420	2.419
G111-DAC-3	D1	0.921	32.702	95.103	0.278	347.708	4.316	6.531	15.001	2.355
G111-DAC-4	D1	0.698	50.248	113.612	0.274	404.201	4.282	6.522	26.465	2.515
G111-DAC-5	D1	0.697	60.308	129.400	0.272	457.292	4.270	6.526	33.266	2.579
G111-DAC-6	D1	0.767	22.551	68.458	0.306	251.282	4.173	6.235	10.058	2.189
G111-DAC-7	D1	0.731	32.300	86.454	0.294	313.517	4.205	6.325	16.236	2.322
X011-DAC-1	D2	0.722	38.080	90.631	0.277	324.444	4.225	6.440	18.329	2.424
X011-DAC-2	D2	0.697	23.380	49.860	0.331	176.058	3.903	5.873	11.736	2.194
X011-DAC-3	D2	0.797	33.036	89.692	0.288	325.732	4.221	6.403	15.822	2.359
G101-MS-1	M	0.437	3.729	11.596	0.561	42.654	3.225	4.368	1.958	1.422
G101-MS-2	M	0.382	6.402	21.016	0.525	77.661	3.402	4.683	3.784	1.562
G101-MS-3	M	0.425	3.533	11.240	0.577	41.425	3.212	4.305	1.912	1.396
G101-MS-4	M	0.515	6.625	16.983	0.474	61.308	3.425	4.866	3.308	1.654
G111-RAC-1	R	1.056	89.744	322.798	0.222	1201.449	4.860	7.374	49.861	2.724
G111-RAC-2	R	1.055	56.364	203.881	0.252	759.159	4.652	7.038	28.584	2.570
G111-RAC-3	R	0.931	60.131	233.693	0.242	874.639	4.753	7.167	30.248	2.598
G111-RAC-4	R	0.969	59.708	169.840	0.263	619.653	4.535	6.886	32.627	2.563
G111-RAC-5	R	1.206	90.112	362.904	0.219	1361.502	4.937	7.465	48.222	2.746
G111-RAC-6	R	1.081	80.810	250.441	0.233	920.955	4.735	7.210	43.486	2.710
G101-SMA-1	S	0.714	55.616	116.891	0.314	411.946	4.249	6.407	33.308	2.480
G101-SMA-2	S	1.056	75.262	242.433	0.227	894.469	4.746	7.256	37.975	2.697
G101-SMA-3	S	1.086	74.427	284.957	0.228	1065.401	4.843	7.319	37.991	2.686
G101-SMA-4	S	0.848	58.265	171.771	0.258	628.820	4.514	6.863	30.161	2.576
G101-SMA-5	S	0.806	38.325	121.577	0.286	447.982	4.368	6.569	18.936	2.408
G101-UTWC-1	U2	0.982	91.929	185.818	0.188	651.343	4.611	7.295	41.412	2.849
G101-UTWC-2	U2	0.985	103.927	226.207	0.192	800.900	4.670	7.345	50.090	2.883
G101-UTWC-3	U2	1.086	125.795	246.702	0.163	861.011	4.769	7.617	57.420	2.985
G101-UTWC-4	U2	1.119	100.295	202.373	0.181	709.198	4.654	7.397	44.965	2.893
G101-UTWC-5	U1	0.870	46.076	103.614	0.246	368.380	4.339	6.716	21.453	2.511
G101-UTWC-6	U1	0.873	46.630	116.142	0.258	417.938	4.366	6.710	22.848	2.496
G101-UTWC-7	U1	0.919	62.951	142.093	0.224	505.421	4.493	6.995	29.660	2.651
G101-UTWC-8	U1	0.930	56.632	138.049	0.227	495.563	4.440	6.889	26.525	2.602
JCXL-OGFC-1	O	1.276	97.943	412.791	0.193	1553.221	5.063	7.804	45.617	2.844
JCXL-OGFC-3	O	1.300	132.609	526.880	0.172	1974.912	5.174	8.046	62.472	2.988
JCXL-OGFC-4	O	1.259	141.717	493.719	0.179	1833.157	5.105	7.962	70.507	3.000
JCXL-OGFC-5	O	1.223	120.946	444.796	0.182	1658.236	5.083	7.901	57.870	2.939

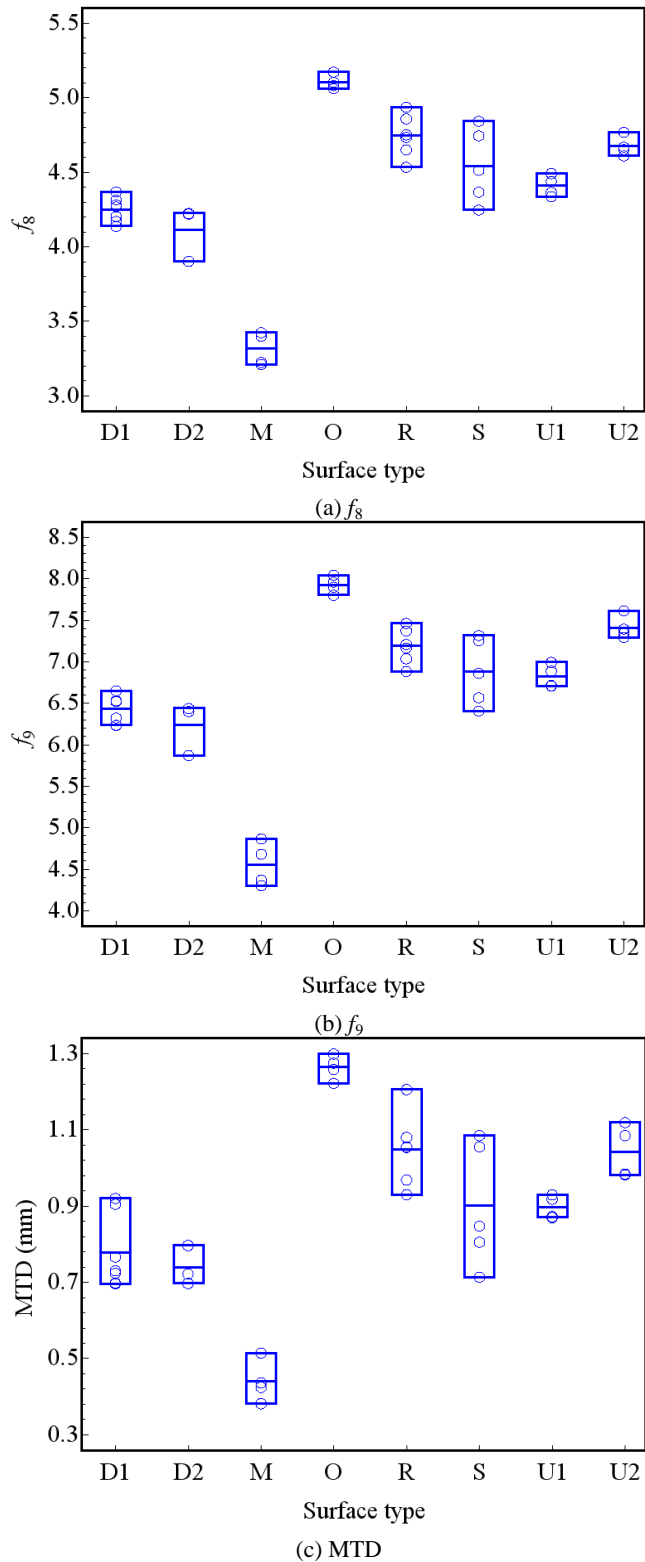


Fig. 6. Distribution of  $f_8$ ,  $f_9$ , and MTD.

exponential models with  $f_8$  and  $f_9$  are presented in Tables 6 and 7 respectively. The exponential models are also highly significant and have smaller MSEs than the linear models. The MSEs of the exponential models with  $f_8$  and  $f_9$  are 0.00343 and 0.00351 which are 23.9% and 38.4% less than the corresponding linear model

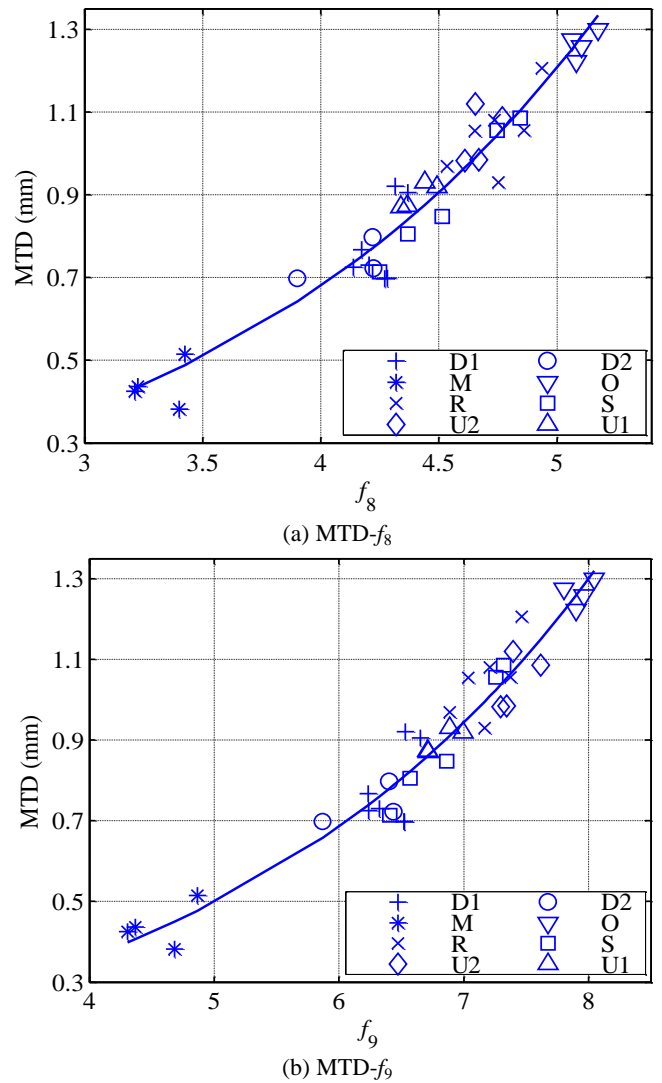


Fig. 7. Scatter Plots of MTD Against  $f_8$ , and  $f_9$  with the Exponential Regression Model.

Table 4. Analysis of Variance for the Linear Model with  $f_8$ .

Source	Degree of Freedom	Sum of Squares	Mean Square	F Value	Pr > F
Model	1	1.8591	1.8591	412.39	<.0001
Error	35	0.1578	0.00451	/	/
Corrected Total	36	2.0169	/	/	/

Table 5. Analysis of Variance for the Linear Model with  $f_9$ .

Source	Degree of Freedom	Sum of Squares	Mean Square	F Value	Pr > F
Model	1	1.8175	1.8175	319.04	<.0001
Error	35	0.1994	0.0057	/	/
Corrected Total	36	2.0169	/	/	/

respectively. The exponential models are better option to relate the 2 GLCM indicators to MTD. The fitted curves based on Eqs. (9) and (10) are depicted in the Fig. 7(a) and Fig. 7(b) respectively.

**Table 6.** Analysis of Variance for the Exponential Model with  $f_8$ .

Source	Degree of Freedom	Sum of Squares	Mean Square	F Value	Approximate Pr > F
Model	2	31.4114	15.7057	4572.73	<.0001
Error	35	0.1202	0.00343	/	/
Uncorrected Total	37	31.5316	/	/	/

**Table 7.** Analysis of Variance for the Exponential Model with  $f_9$ .

Source	Degree of Freedom	Sum of Squares	Mean Square	F Value	Approximate Pr > F
Model	2	31.4087	15.7043	4471.97	<.0001
Error	35	0.1229	0.00351	/	/
Uncorrected Total	37	31.5316	/	/	/

$$MTD = 0.0683 \times e^{0.5745 f_8} \quad (9)$$

$$MTD = 0.1004 \times e^{0.3201 f_9} \quad (10)$$

## Discussion

According to the definition of Shannon information measure [33], the amount of information of an event with probability  $p$  is  $-\log(p)$ , which increases with the decrease of  $p$ . In this work, all of the 3-D macrotecture measurements have an equal number of pixel pairs with given spatial relationship for the same size of the measurements. However, the number of gray level combinations and sums of pixel pair depends on  $N_g$ , which corresponds to the height range of the 3-D macrotecture. A bigger  $N_g$ , corresponding to a bigger height range of the 3-D macrotecture, means larger numbers of gray level combinations and sums of pixel pair and then lower  $P_d^\theta(i, j)$  and  $P_{x+y}(k)$  for the constant pixel pair number. The lower  $P_d^\theta(i, j)$  and  $P_{x+y}(k)$ , the bigger the corresponding amount of information. Therefore the macrotecture with bigger height range has relatively large  $f_9$  and  $f_8$ , which are the average amount of information of the gray level combination distribution and the gray level sum distribution respectively.

According to the property of entropy [33], the possible ranges of  $f_8$  and  $f_9$  are  $[0, \log(2N_g - 1)]$  and  $[0, 2\log(N_g)]$  respectively. For a flat surface, there is only 1 gray level combination and 1 gray level sum which results in a value of 0 for  $f_8$  and  $f_9$ . The maximums of  $f_9$  and  $f_8$  will be obtained only when all gray level combinations and all gray level sums of pixel pairs have the same probability respectively [33]. And the bigger  $N_g$ , the larger the maximums of them. Generally, the macrotecture becomes more complex with the growth of  $f_8$  and  $f_9$ . It should be noted that the value of  $N_g$  for a given macrotecture depends on the height interval used in mapping height onto gray level in accordance with Eq. (6). So the values of  $f_8$  and  $f_9$  are related to the height interval. The same height interval should be taken to ensure consistency of the results.

## Conclusions

This paper employs the GLCM features to quantify 3-D macrotecture characteristics of asphalt pavement through mapping its heights onto a set of gray levels. Test data collected at 37 highway and urban road sections, including 6 types of surface layers in asphalt pavement, i.e., DAC, SMA, RAC, UTWC, MS, and

OGFC, are analysed. The conclusions can be drawn as follows.

The PPO does not have significant influence on the GLCM indicators of asphalt pavement 3-D macrotecture, for asphalt pavement surface is statistically rotation invariant. However, most GLCM indicators are PPD dependent. It is recommended to use the average in the 2 PPOs (horizontal and vertical) and the 4 PPDs (0.5 mm through 2 mm by 0.5 mm) as each indicator's final value for connecting with MTD.

There are 2 GLCM indicators,  $f_8$  and  $f_9$ , have strong relationship with MTD, between which and MTD the correlation coefficients are 0.9601 and 0.9493 respectively. The 2 GLCM indicators are entropy of the gray level sum distribution and the gray level combination distribution of pixel pairs of pavement macrotecture respectively, which describe the average amount of information of the corresponding distribution. The larger the values of  $f_8$  and  $f_9$ , the more complex of the pavement macrotecture, which means bigger height range and more even distributions of the gray level sum and the gray level combination.

Regression analysis shows that the exponential models are better choice for connecting  $f_8$  and  $f_9$  with MTD. The MSEs of the exponential models with  $f_8$  and  $f_9$  are 0.00343 and 0.00351 respectively and all the exponential models are highly significant.

## Acknowledgement

The research reported in this paper is funded by the National Natural Science Foundation of China (No. 50908004 and No. 51178013).

## References

- Perez-Jimenez, F., Martinez, A., Sanchez-Dominguez, F., and Ramos-Garcia, J.A. (2011). System for measuring splash on wet pavements, *Transportation Research Record*, No. 2227, pp. 171-179.
- Henry, J.J. (1978). The Relationship between texture and pavement friction, *Tire Science and Technology*, 6(4), pp. 215-232.
- Piarc (1987). Technical Committee Report No 1: Surface Characteristics, *XVIII World Road Congress*, Brussels, Belgium.
- Ongel, A. and Harvey, J. (2010). Pavement characteristics affecting the frequency content of tire/pavement noise, *Noise Control Engineering Journal*, 58(6), pp. 563-571.

5. Cackler, E.T., Ferragut, T., and Harrington, D.S. (2006). *Evaluation of U.S. and European Concrete Pavement Noise Reduction Methods*, National Concrete Pavement Technology Center, Iowa State University, Ames, IA, USA.
6. Abbas, A., Kutay, M. E., Azari, H., and Rasmussen, R. (2007). Three-dimensional surface texture characterization of Portland cement concrete pavements, *Computer-Aided Civil and Infrastructure Engineering*, 22(3), pp. 197-209.
7. Ech, M., Yotte, S., Morel, S., Breysse, D., and Pouteau, B. (2007). Laboratory evaluation of pavement macrotexture durability, *Revue Européenne de Génie Civil*, 11(5), pp. 643-662.
8. Gendy, A.E. and Shalaby, A. (2007). Mean profile depth of pavement surface macrotexture using photometric stereo techniques, *Journal of Transportation Engineering*, 133(7), pp. 433-440.
9. Gendy, A.E., Shalaby, A., Saleh, M., and Flintsch, G.W. (2011). Stereo-vision applications to reconstruct the 3D texture of pavement surface, *International Journal of Pavement Engineering*, 12(3), pp. 263-273.
10. Vilaca, J.L., Fonseca, J.C., Pinho, A.M., and Freitas, E. (2009). A new machine for acquire pavement texture. *IEEE 7th International Conference on Computational Cybernetics*, Palma de Mallorca, Spain, pp. 97-102.
11. Wen, J. (2009). Study on Evaluating Texture Depth of Asphalt Pavement with Digital Technology, Chang'an University, Xi'an, China.
12. Bitelli, G., Simone, A., Girardi, F., and Lantieri, C. (2012). Laser scanning on road pavements: a new approach for characterizing surface texture, *Sensors*, 12, pp. 9110-9128.
13. Sengoz, B., Topal, A., and Tanyel, S. (2012). Comparison of pavement surface texture determination by sand patch test and 3D laser scanning, *Periodica Polytechnica: Civil Engineering*, 56(1), pp. 73-78.
14. Wang, K.C.P. and Li, L. (2012). Pavement Surface Texture Modeling Using 1mm 3D Laser Images, *Transportation Systems Workshop 2012*, Austin, TX, USA.
15. Laurent, J., Hébert, J.F., Lefebvre, D., and Savard, Y. (2012). Using 3D laser profiling sensors for the automated measurement of road surface conditions, *7th RILEM International Conference on Cracking in Pavements*, Delft, Netherlands, pp. 157-168.
16. Haralick, R.M., Shanmugam, K., and Dinstein, I. (1973). Textural features for image classification, *IEEE Transactions on Systems, Man, and Cybernetics*, SMC-3(6), pp. 610-621.
17. Clausi, D.A. (2002). An analysis of co-occurrence texture statistics as a function of gray level quantization, *Canadian Journal of Remote Sensing*, 28(1), pp. 45-62.
18. Ayyachamy, S. and Vasuki, M. (2013). Content based medical image retrieval for histopathological, CT and MRI images, *Applied Medical Informatics*, 33(3), pp. 33-45.
19. Zulpe, N. and Pawar, V. (2012). Glcm textural features for brain tumor classification, *International Journal of Computer Science Issues*, 9(3), pp. 354-359.
20. Soh, L. and Tsatsoulis, C. (1999). Texture analysis of Sar sea ice imagery using gray level co-occurrence matrices, *IEEE Transactions On Geoscience And Remote Sensing*, 37(2), pp. 780-795.
21. Miao, Y., Song, P., and Gong, X. (2014). Fractal and multifractal characteristics of 3-D asphalt pavement macrotexture, *Journal of Materials in Civil Engineering*, 26(8), pp.04014033-1:11.
22. Haralick, R.M. (1979). Statistical and structural approaches to texture, *Proceedings of the IEEE*, 67(5), pp. 786-804.
23. Eleyan, A., and Demirel, H. (2011). Co-occurrence matrix and its statistical features as a new approach for face recognition, *Turkish Journal of Electrical Engineering & Computer Sciences*, 19(1), pp. 97-107.
24. Theodoridis, S. and Koutroumbas, K. (2009). *Pattern Recognition*, 4th edition, Academic Press, Burlington, MA, USA.
25. Weszka, J.S., Dyer, C.R., and Rosenfeld, A. (1976). A comparative study of texture measures for terrain classification, *IEEE Transactions on Systems, Man, and Cybernetics*, SMC-5(4), pp. 269-285.
26. Zucker, S. W., and Terzopoulos, D. (1980). Finding structure in co-occurrence matrices for texture analysis, *Computer Graphics and Image Processing*, 12(3), pp. 286-308.
27. Conners, R.W. and Harlow, C.A. (1980). A theoretical comparison of texture algorithms, *IEEE Transactions on Pattern Analysis and Machine Intelligence*, PAMI-2(3), pp. 204-222.
28. Holmes, Q.A., Nuesch, D.R., and Shuchman, R.A. (1984). Textural analysis and real-time classification of sea-ice types using digital Sar data, *IEEE Transactions on Geoscience and Remote Sensing*, 22(2), pp. 113-120.
29. Chen, D.W., Sengupta, S.K., and Welch, R.M. (1989). Cloud field classification based upon high spatial resolution textural features: 2. simplified vector approaches, *Journal of Geophysical Research: Atmospheres*, 94(D12), pp. 14749-14765.
30. Nystuen, J.A. and Garcia Jr., F.W. (1992). Sea ice classification using Sar backscatter statistics, *IEEE Transactions on Geoscience and Remote Sensing*, 30(3), pp. 502-509.
31. Rao, C.N., Sastry, S.S., Mallika, K., Tiong, H.S., and Mahalakshmi, K.B. (2013). Co-occurrence matrix and its statistical features as an approach for identification of phase transitions of mesogens, *International Journal of Innovative Research in Science, Engineering and Technology*, 2(9), pp. 4531-4538.
32. Shokr, M.E. (1991). Evaluation of second-order texture parameters for sea ice classification from radar images, *Journal of Geophysical Research*, 96(C6), pp. 10625-10640.
33. MacKay, D.J.C. (2003). *Information Theory, Inference, and Learning Algorithms*, Cambridge University Press, Cambridge, UK.